Near-zero-index platform in photonics: tutorial

Vertchenko, Larissa; Nikitin, Maxim; Laurynenka, Andrei

Published in:
Journal of the Optical Society of America B: Optical Physics

Link to article, DOI:
10.1364/JOSAB.489055

Publication date:
2023

Document Version
Publisher's PDF, also known as Version of record

Journal of the Optical Society of America B
OPTICAL PHYSICS

Near-zero-index platform in photonics: tutorial

LARISSA VERTCHENKO,[1,2] MAXIM NIKITIN,[1] AND ANDREI LAVRINENKO[1,*]

[1]Department of Electric and Photonics Engineering, Technical University of Denmark, Ørsteds Plads 345A, DK-2800 Kgs. Lyngby, Denmark
[2]Currently with Sparrow Quantum Ltd., Copenhagen, Denmark
*alav@dtu.dk

Received 1 March 2023; revised 12 April 2023; accepted 19 April 2023; posted 20 April 2023; published 4 May 2023

The need for miniaturization and faster communications resulted in the rise of photonics, with the big promise of light circuits with high speed and low heating. Near-zero-index materials have gained attention due to their peculiar electromagnetic properties, such as enhancement of the electric field and extraordinary transmission inside photonic waveguides. Furthermore, in such a medium, light propagates with constant phase, thus holding great promise for the field of quantum photonics, where information is preserved instead of degraded by the environment, causing decoherence. However, its realization still remains challenging, as it requires very specific geometries to fulfill some requirements related to the effective medium theory. In this tutorial, we present a theoretical overview of low-index materials' most intriguing yet useful characteristics and their prospective applications.

https://doi.org/10.1364/JOSAB.489055

1. INTRODUCTION

The miniaturization capability and efficiency of electronic devices have reached the limit regarding power consumption due to intrinsic material losses and Ohmic heating. As a result, the field of photonics has emerged as a promise to substitute microelectronics using mainly optical components, such as optical fibers, waveguides, and light sources. Just as new prospects towards light circuits come into play, so do their challenges. As light interacts with matter, even though Ohmic heating is to some extent overcome, propagation losses and optical effects such as absorption, reflection, diffraction, emission, and scattering appear. Although these effects may be relevant for some experiments, they may also be undesirable for others, as they act as dissipation channels of radiation, and the information that is supposed to be transmitted gets lost. As a consequence, research on not only materials' intrinsic properties but also engineering becomes necessary to optimize photonic systems' performance. In this context, near-zero (refractive)-index (NZI) materials bear great potential to allow new features in manipulation with light wave propagation in photonic chips. For instance, spatial and temporal characteristics of electromagnetic waves inside an NZI material can be decoupled. This can be observed through the wave equation, which describes a propagating wave by

$$\nabla^2\mathbf{E} - \frac{\varepsilon\mu}{c^2}\frac{\partial^2\mathbf{E}}{\partial t^2} = 0, \tag{1}$$

showing the dependence of the field propagation on the relative materials' dielectric permittivity and magnetic permeability, ε and μ, respectively. Considering propagation along one direction, for example, along x axis [wave vector $\mathbf{k} = (k_x, 0, 0)$], the solution to Eq. (1) is a plane wave with the exponential part related to the material parameters by

$$E = E_0 e^{i\sqrt{\varepsilon\mu}k_0 x} = E_0 e^{ik_x x}, \tag{2}$$

where $k_x = \sqrt{\varepsilon\mu}k_0$, $k_0 = \omega/c$, and ω is an angular frequency. By looking at the wave Eq. (1), when ε and μ become small, the temporal term becomes negligible, reducing Eq. (1) to Laplace's equation $\nabla^2 E = 0$, which governs electrostatics. It effectively means that the field has a constant amplitude in space while dynamically oscillating in time [1]. Therefore, there is an apparent decoupling between spatial and temporal parts that describe the electromagnetic field dynamics. We can find implications of such an effect in engineering novel resonant cavities. The wave equation solutions for a specific cavity depend on the boundary conditions, resulting in cavities operation with a fixed resonant frequency for a particular shape and size. By decoupling spatial and temporal components of the electromagnetic field, it is possible to find the same resonance frequency values for different cavity configurations. Such invariance of the resonance frequency concerning geometrical transformations is well suited for applications with deformable and flexible photonics [2].

The rest of the paper is divided into the following sections. Section 2 deals with the classification of material properties of NZI materials. Sections 3 and 4 describe the ray-optics and wave-optics properties of NZI materials. Implications of NZI media in quantum photonics are discussed in Section 5, while nonlinear optics with NZI materials is the topic of Section 6, followed by conclusions.

2. CLASSIFICATION OF NZI MATERIALS

We start this tutorial by focusing on the fundamental properties of electromagnetic radiation propagating inside uniform NZI materials. For simplicity, we take first only the real optical constants. Electromagnetic properties of materials are associated with relative permittivity ε and permeability μ. To differentiate between vanishing electric and magnetic constants, we refer to materials with $\varepsilon \to 0$ as epsilon-near-zero (ENZ), with $\mu \to 0$ as mu-near-zero (MNZ), and with both of them tending to zero as epsilon-mu-near zero (EMNZ) [3]. The properties of propagating waves are connected with the refractive index or wavenumber (propagation constants). According to the relation connecting the refractive index to electromagnetic constants $n = \sqrt{\varepsilon\mu}$, materials classified as EMNZ must populate the intersection area of ENZ and MNZ materials [Fig. 1(a)], that is, the square of sizes 2×2 around the origin of the coordinate system with an axis representing the real permittivity and permeability values [Fig. 1(a)]. As we plot only the upper part of the μ-subspace, EMNZ materials occupy only the upper half of the square. When the refractive index gets significantly lower than one in absolute value, the more appropriate it is to label such materials as NZI materials. In the absence of losses, i.e., when permittivity and permeability are real, all three cases are almost identical to the NZI configuration as showcased by the deep blue color field in Fig. 1(a). The yellow-colored field marks the region where $n > 1$. Following such a simplified approach, there is an abundant amount of ENZ materials; see the vertical white dashed line in Fig. 1(a). Examples are noble metals, such as gold (Au), silver (Ag), and copper (Cu), and other kinds of metals such as aluminum (Al) and doped semiconductors. Typically, these materials exhibit plasmonic properties, for example, concentrating light on nanoscopic scales.

In reality, all aforementioned materials are well described by the Drude or more elaborate Drude–Lorentz model for complex permittivity ε. When the imaginary part of the permittivity is added to the system, we can see big changes in the $n \lesseqgtr 1$ regions, as shown in Fig. 1(b). The real part of a Drude metal permittivity attains zero value in the zero-crossing point close to the plasma frequency [4]. Nonetheless, metals do not expose low refractive indices in the visible range [5]. These limitations triggered the search for novel plasmonic materials. For the visible range, transition nitrides, such as titanium nitride (TiN) and zirconium nitride (ZrN), are quoted as valuable substitutes for Au and Ag due to their plasmonic properties. They have the advantage of being CMOS compatible [6]. For the infrared range, transparent conductive oxides such as indium tin oxide (ITO) and gallium- (GZO) and aluminum-doped zinc oxides (AZO) are preferable materials. However, they still have high intrinsic losses and cannot be strictly considered NZI, as all-optical effects related to a near-zero refractive index are worsened. An interesting illustration between the real and imaginary parts of material parameters is given in [7], where the coordinates were chosen as $\Re(n) \equiv n'$ versus $\Im(n) \equiv n''$, and material dispersion is reflected as curvilinear lines in these coordinates for some important materials such as Au, TiN, SiN, AZO, ITO, and GZO.

What will be the implications of taking materials with parameters from the blue highlighted areas in Fig. 1? According to the constitutive relations

$$\mathbf{D} = \varepsilon_0 \varepsilon \mathbf{E}, \tag{3a}$$

$$\mathbf{B} = \mu_0 \mu \mathbf{H}, \tag{3b}$$

the induced polarization $\mathbf{P} = \mathbf{D} - \varepsilon_0 \mathbf{E}$ and magnetization $\mathbf{M} = \mathbf{B}/\mu_0 - \mathbf{H}$ can compensate for external electric $\mathbf{E}$ and magnetic $\mathbf{H}$ fields. A small refractive index value means that phase velocity $v = c/n$ exceeds the speed of light in vacuum, and correspondingly, wavelength λ of the propagating waves is much extended over the vacuum dimension. In the limited case of $\varepsilon = 0$, the wavelength becomes infinite, providing in-phase oscillations of the local electric field in all space occupied by such material; see Fig. 2. The temporal behavior of the electric and magnetic fields in the case of ENZ and MNZ media is not disturbed, while the amplitude of complementary fields (magnetic for the ENZ and electric for the MNZ) is constant and without loss of generality may be nullified. As seen previously, the EMNZ medium supports time-varying but spatially invariant

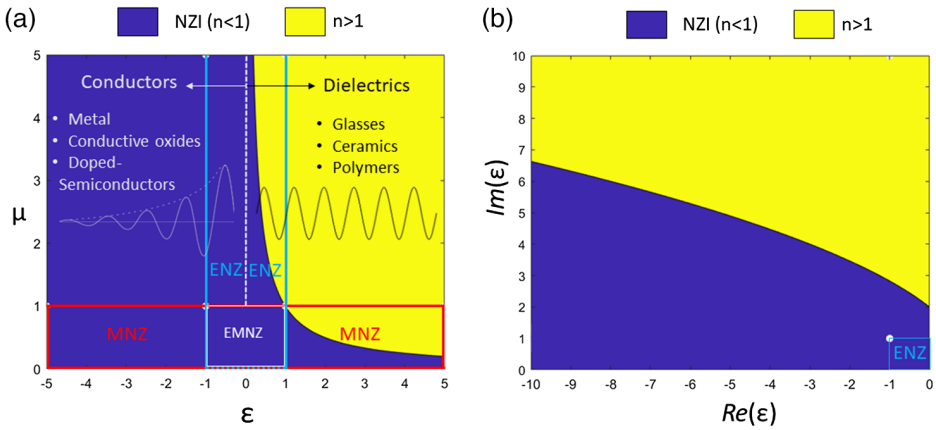

Fig. 1. (a) Plot of the transition between conductors and dielectrics with their respective propagation properties, where the NZI region is highlighted in deep blue and regions with a refractive index above one are highlighted in yellow. The EMNZ region with ε between -1 and $+1$ is delimited by the white line. The ENZ and MNZ regions are delimited by blue and red lines, respectively. The negative μ semi-space is not shown for compactness. (b) Plot of the dependence of the absolute value of the refractive index as a function of permittivity ε when adding losses to the material $\Im(\varepsilon)$.

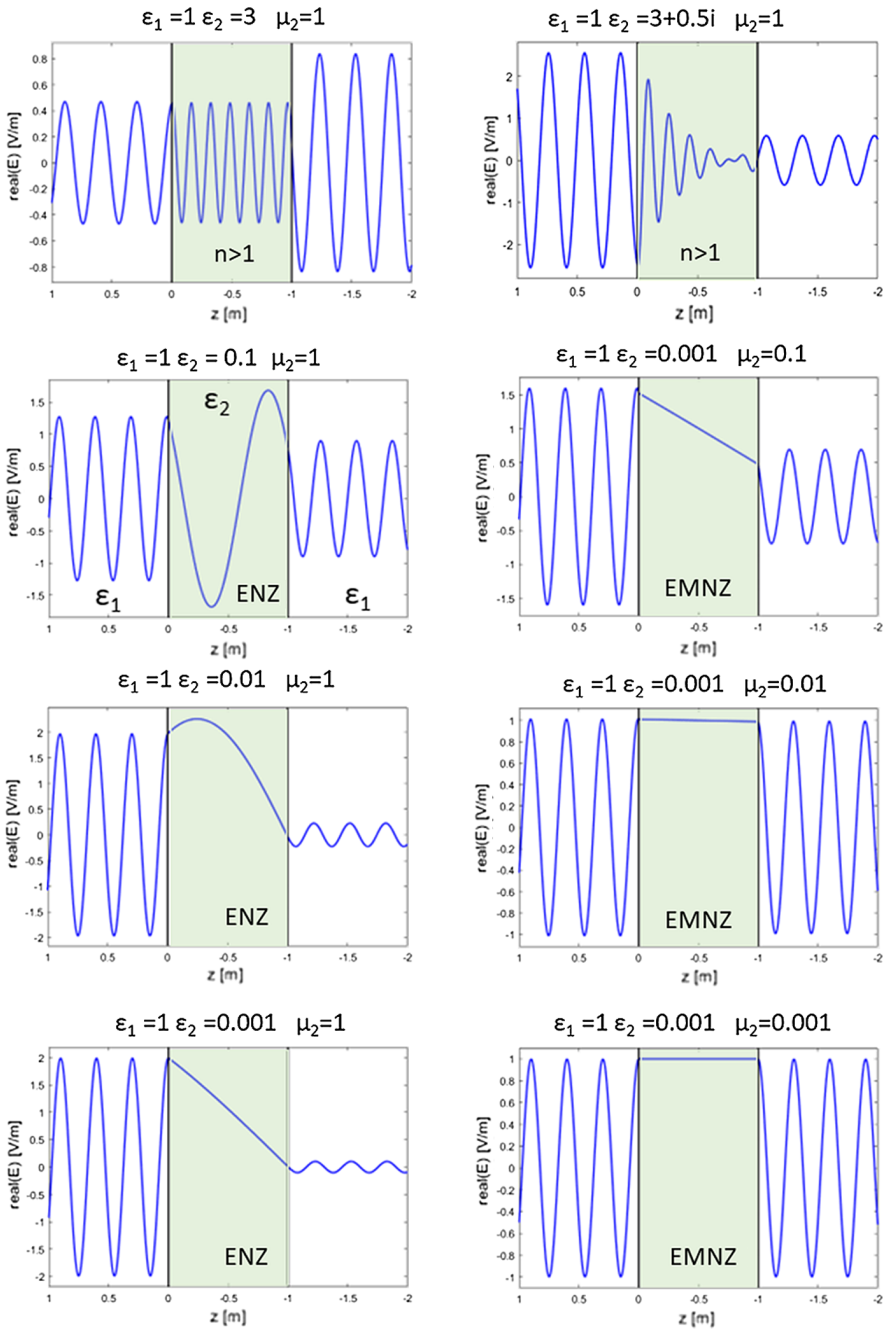

Fig. 2. Illustration of the difference between the wavelength in a conventional dielectric with $\varepsilon > 1$ and zero-index materials (ENZ left and EMNZ right), where the wavelength becomes infinite when $\varepsilon \to 0$.

electromagnetic fields in all internal volumes independent of their sizes and shapes.

As discussed previously, there are different classes of materials such as ENZ, MNZ, EMNZ, and NZI, depending on the values of ε, μ, and, correspondingly, n. Normally, the permeability is related to magnetic fields with applications in electronics by manipulating inductance and capacitance. However, MNZ materials are not easily found in the optical frequency range. One way to tailor materials' permeability is by adding dielectric particles acting as dopants, as described in [8]. Such impurities modify the effective permeability being able to reach extremely low values. As many optical effects studied in this tutorial are related mostly to the electric field, we will give more emphasis to ENZ materials.

For negligible losses, which are related to the vanishing imaginary parts of their material parameters, all classes stand for sufficient conditions to be referred to as NZI materials. However, such an approximation is crude, as it completely ignores dispersion. By definition, dispersion occurs when material properties of the medium, such as ε and μ, depend on the frequency. To account for dispersion properties, one needs to accept complex permittivity and permeability functions

obeying the Kramers–Kronig relations [9]. For example, the imaginary part of the permittivity in the Drude model is associated with electron scattering through the collision frequency parameter. In turn, the imaginary part of ε contributes to the imaginary part of the mode propagation constant, i.e., the imaginary part of the refractive index in the case of plane waves in a homogeneous medium. As a consequence, the refractive index will be different from zero even if the real part of the permittivity is zero. Hence, as exemplified below, the ENZ condition loses sense as a sufficient condition of the NZI case.

To elaborate on this point, we look at some ENZ examples described by the Drude model and compare their optical properties on ENZ and NZI wavelengths. As $\mu = 1$ is a very good approximation at optical frequencies, complex permittivity and refractive index

$$\varepsilon = \varepsilon' + i\varepsilon'', \tag{4a}$$

$$n = n' + in'' \tag{4b}$$

are connected through $n = \sqrt{\varepsilon}$. That gives

$$n' = \sqrt{\frac{\sqrt{\varepsilon'^2 + \varepsilon''^2} + \varepsilon'}{2}}, \tag{5a}$$

$$n'' = \sqrt{\frac{\sqrt{\varepsilon'^2 + \varepsilon''^2} - \varepsilon'}{2}}. \tag{5b}$$

In the case of the zero-crossing point, $\varepsilon' = 0$; thus, the real and imaginary parts of the refractive index are equalized $n' = n'' = \sqrt{\varepsilon''/2}$. However, it does not automatically mean that $\Re(n)$ reaches the minimum. To exemplify this statement, we use the ellipsometry dataset for the ITO samples from [5]. There is a pronounced difference between the ENZ wavelength $\lambda_{\mathrm{ENZ}} = 1402$ nm and the wavelength of the smallest real part of the refractive index at $\lambda_{\mathrm{NZI}} = 1681$ nm. The refractive indices are $n_{\mathrm{ENZ}} = 0.832 + i0.832$ and $n_{\mathrm{NZI}} = 0.612 + i0.919$. While the latter case brings more losses in the propagation of plane waves, it enables higher efficiency of nonlinear optical effects. Such a discrepancy between ENZ and NZI wavelengths is also observed in the aforementioned plot in [7], as typically the lowest point on the coordinate axis ($\Re(n)$) is shifted away from the highlighted ENZ zone.

ITO is notorious for having its material properties governed by geometrical parameters, i.e., the thickness of layers and fabrication method. Thus, we use another dataset for ITO from [10]. The advantage of such data is that the authors claim that the permittivity of the 300 nm thick layer of ITO is accurately described by the Drude model with parameters $\varepsilon_\infty = 3.8055$, $\omega_p = 2\pi \cdot 473 \cdot 10^{12}\ \mathrm{s}^{-1}$, $\gamma = 0.0468\omega_p$. With such parameters, $\lambda_{\mathrm{ENZ}} = 1241$ nm, while $\lambda_{\mathrm{NZI}} = 1511$ nm. As mentioned in a recent paper [11], the spin–orbit interactions facilitated by the ITO film do not occur at the wavelength λ_{ENZ}, but at the wavelength redshifted by 80 nm towards lower $\Re(n)$.

An additional example that illustrates a negative result in a claim for NZI properties is TiN. Due to its plasmonic behavior, TiN has been pointed out as an alternative ENZ material for the visible range [4]. The permittivity of TiN also greatly depends on the fabrication method and thickness of the sample, most

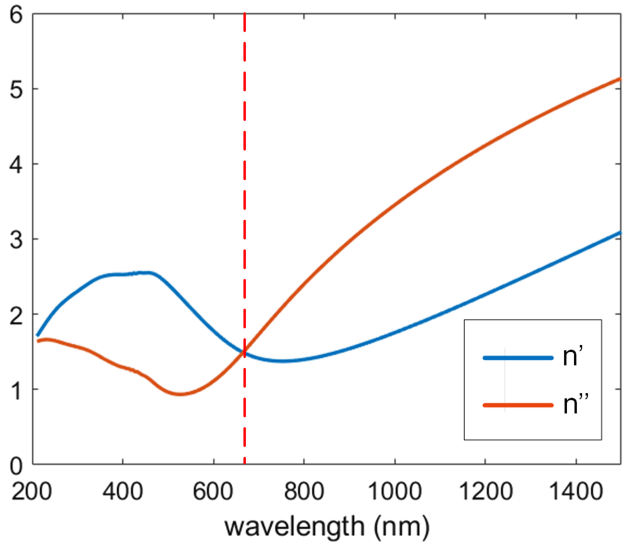

Fig. 3. Real (n') and imaginary (n'') parts of the refractive index for a 100 nm thin film of titanium nitride as a function of wavelength, exemplifying the dispersion properties of such a medium. The red dashed line designates the zero-crossing point $\Re(\varepsilon) = 0$.

experiments having been conducted at room temperature or above [12,13]. As shown in Fig. 3 a 100 nm TiN film exhibits the zero-crossing point of the real part of permittivity in the visible range [14]. However, its large imaginary part heavily contributes to the refractive index, especially at the zero-crossing point, where $n' = n'' = \sqrt{\varepsilon''/2} \simeq 1.5$, Fig. 3. Hence, it is clear that, despite the zero-crossing point, such material cannot be considered NZI. Moreover, significant losses prevent using such material at the ENZ wavelength in optical circuits. Another consequence, which we emphasized with the aforementioned ITO example, is a pronounced distinction in wavelengths, where $\Re(\varepsilon)$ and $\Re(n)$ reach the minimal values (670 nm versus 800 nm).

As an attempt to ameliorate the performance of ENZ TiN films, their reflection was characterized as a function of temperature decreasing from room temperature to cryogenic values [15]. We can observe a slight gradual increase in the zero-crossing wavelength as temperature decreases to ∼4 K. This is associated with counteracting effects of the electron density and effective mass reduction as discussed in [13]. The imaginary part of ε linearly decreases with temperature fitted in the range from 4 K to 200 K by the function $0.0056T + 1.37$. Even for points excluded from the fit for temperatures reaching $T = 1.5$ K, the imaginary part is still around 1.0.

As described previously, the intrinsic losses related to conductors make dielectric platforms highly desirable. An alternative approach to achieve an effective index near-zero regime using structured materials in a more or less extended frequency range relies on photonic crystals. Such periodic structures have discrete translation symmetry with lattice sizes close to the free space wavelength of interest. We recall that, by definition, permittivity is a measure of the polarizability of charges in the presence of an electric field, with each atom behaving as an electric dipole. In the case of discrete objects that compose a unit cell of a photonic crystal, such as pillars, these polarized dipoles

collectively yield scattered radiation behaving as nanoscale resonators. The radiation emitted by several dipoles interferes and forms specific field profiles depending on the structure's size and shape. Such patterns are known as Mie resonances [16,17], and the full description of nanoparticle excitation dependent on the frequency is given by the Mie scattering theory [18]. It is possible to tune the mode profiles, such as of a dipole, a monopole, and other higher-order modes, for the desired frequencies by simply adjusting the structural parameters of the unit cell.

To achieve NZI behavior using a photonic crystal platform, the system must be optimized to exhibit eigenmodes degenerated close to the Γ point [19] with specific mode profiles. When the frequency of such electromagnetic modes is linearly proportional to the wave vector at the Brillouin zone boundaries, we can observe a cone-like band structure, commonly referred to as Dirac cones, and the intersection between two cones at ω_0 is called the Dirac point [20]. For a homogeneous material with both $\varepsilon(\omega_0) = 0$ and $\mu(\omega_0) = 0$, the dispersion near ω_0 is linear and associated with Dirac cones. For photonic crystals to exhibit the behavior of effective NZI materials, the Dirac point must have an additional mode [21]. In this particular case, a triple degenerate state is formed. However, some considerations regarding the nature of excited modes must be considered. For a system of pillars to exhibit NZI properties, the three Mie resonances supported by the system must correspond to two dipoles and one monopole, while in the case of membranes, a quadrupole, a dipole, and a monopole or hexapole must coexist [22,23].

For a system consisting of silicon cylinders ($\varepsilon = 12.5$) in a square lattice and embedded in air, with radius $r = 0.2a$ and a being the lattice constant, we obtain the band diagram for transversal magnetic (TM) polarization (electric field along rod axis) with respective electromagnetic modes depicted in Fig. 4, where the yellow circle indicates the triple degeneracy point at Γ. The electromagnetic modes corresponding to the three Mie resonances close to the Dirac point are two dipoles and one monopole [24]. The additional flatband corresponds to a dipole mode.

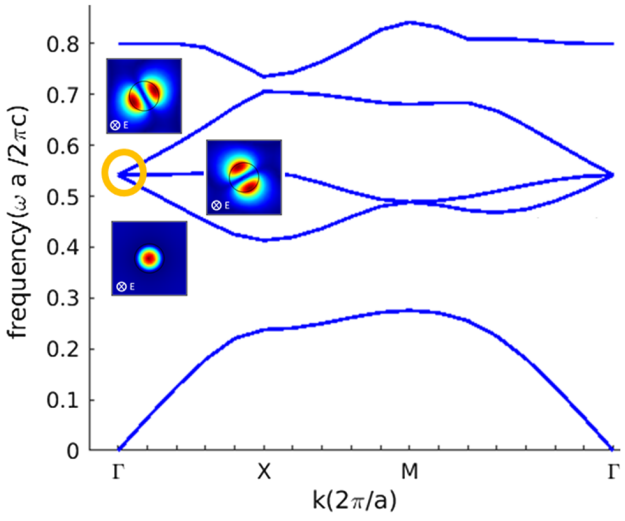

Fig. 4. Band structure for TM polarization of a square lattice of Si ($\varepsilon = 12.5$) pillars with $r = 0.2a$. The yellow circle indicates triple degeneracy at Γ with respective mode profiles along the $\Gamma - X$ direction, corresponding to one monopole and two dipoles. The simulations were performed using the free software *MIT Photonic Bands*.

In the case of pillars, when these specific three modes intercept, we can apply the effective medium theory, and at the triple point's frequency ω_0, the effective constitutive parameters will be $\varepsilon(\omega_0) \approx 0$ and $\mu(\omega_0) \approx 0$. This means that the medium has an effective zero index, although the bulk material (silicon) permittivity is pronouncedly different from zero [21]. Special consideration should be given to the dipole modes excited along the $\Gamma - X$ direction. We notice that they have in-plane magnetic field components in the same direction of k. This means that longitudinal modes are also excited within the system, which disturbs the radiation phase inside the NZI medium, thus losing its uniformity characteristic. One solution to avoid such distortion is to excite only the monopole resonance, shifting the frequency close to the triple point. So, instead of a zero index, we would have an NZI material with properties sufficient to manifest low-index phenomena. A uniform phase pattern brings flexibility in engineering photonic devices, as light experiences neither diffraction nor scattering due to such enlarged wavelengths in NZI materials. A photonic NZI beam splitter composed of three waveguides oriented perpendicularly to each other can still have the same signal intensity in each channel, which is impossible otherwise due to big reflections originated by the impedance mismatch. This is illustrated in Fig. 5 where

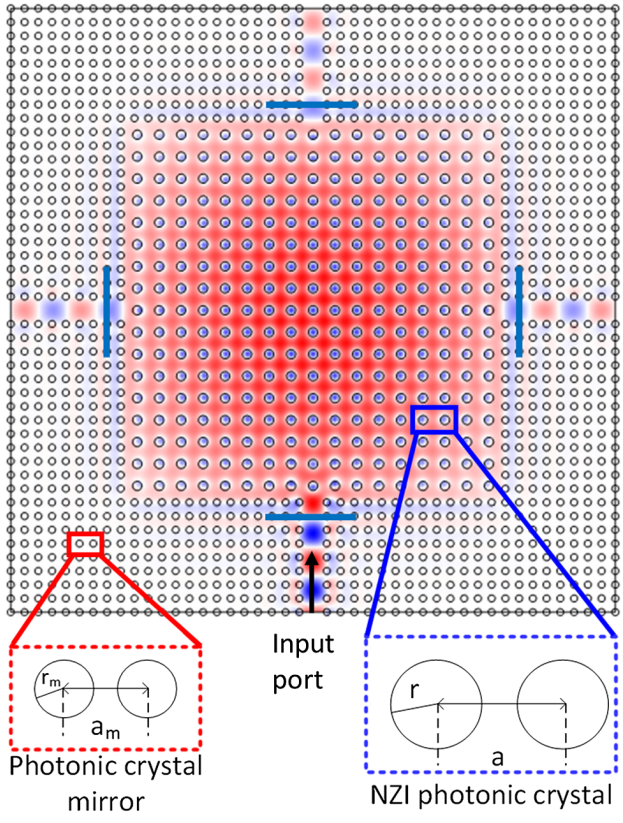

Fig. 5. Illustration of the simulated nonlinear photonic crystal configuration. The system is composed of two regions. An NZI photonic crystal with radius $r = 192$ nm and lattice constant $a = 921$ nm is surrounded by another photonic crystal operating as mirrors with $r_m = 145$ nm and $a_m = 575$ nm. The port excites the system with the fundamental TM mode (out-of-plane magnetic field). All pillars are made of Si. The color scheme indicates the magnetic field amplitude.

a photonic crystal system consists of two regions. First, an NZI photonic crystal made of Si pillars was designed at Dirac's triple point with radius $r = 192$ nm and lattice constant $a = 921$ nm.

The second region is composed of Si pillars designed to have a bandgap at the NZI wavelength, thus working as a mirror. The dimensions of the radius and pitch for the second region are $r_m = 145$ nm and $a_m = 575$ nm. For the sake of the CPU processing time, we took a 2D photonic crystal with sizes 17×17 lattice constants. Four line defects were carved in the second photonic crystal to work as input/output waveguides. Intensity monitors were placed in each waveguide near the NZI region, and a port generates incoming electromagnetic radiation through its fundamental TM mode (out-of-plane magnetic field) at the bottom waveguide.

In that sense, we can try to implement the photonic crystal concept with triple degenerate modes. We check our simulation results by having a uniform phase in a full photonic crystal platform, as depicted in Fig. 5. The mode from the input channel enters the NZI domain and fills it with fields exhibiting uniform phase distribution (colors in the figure designate the modal phases). The important observation is that the modes in all three output waveguides have exactly the same phase irrelevant to the distance they travel inside the NZI patch. Another example of such equiphase behavior inside the NZI domain is shown in Fig. 6. Two rectangular patches (parameters given in the figure caption) are connected with a narrow one-row-thick channel. The fields in both patches and the linking channel between them are completely synchronized with zero phase offset. Inside the narrow channel, we notice a higher electric field, as predicted

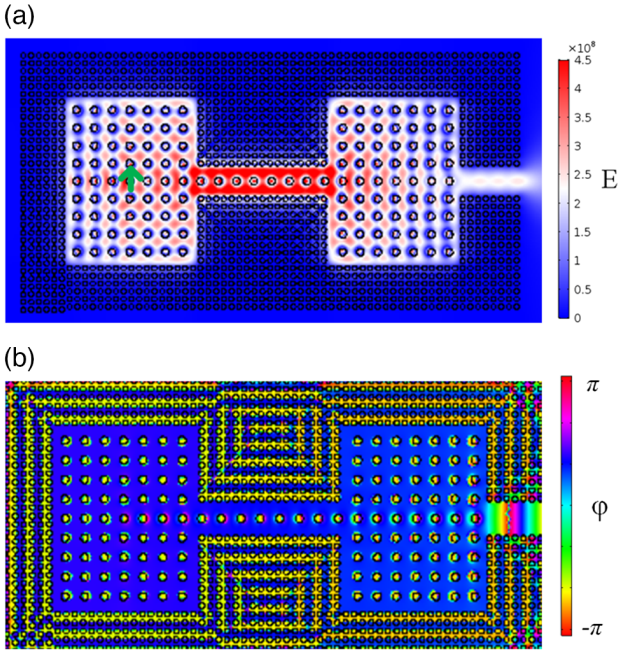

Fig. 6. (a) Supercoupling effect for a photonic crystal platform made of Si pillars ($\varepsilon_r = 12.5$) where the frequency of operation is close to the triple point ($k = 0.002$). The electric field is emitted by a line source placed in the middle of the left cavity (green arrow) at the wavelength of 1530 nm. The structure is surrounded by another photonic crystal with $r = 121$ nm and $a = 367$ nm, providing the mirror effect as its ban gap covers the frequency of the source. (b) Phase distribution of the same system.

for the supercoupling effect due to energy conservation. The system is surrounded by another photonic crystal designed to work as a mirror with $r = 121$ nm and $a = 367$ nm, where the wavelength of the dipole was arranged in the mirror bandgap. Such a system can be employed for several applications such as photonic circuitry and optical sensors [25].

3. RAY-OPTICS PROPERTIES OF NZI MATERIALS

Direct ray-optics features of NZI materials are connected with Snell's law and Fresnel's coefficients when considering the interfaces of such media with conventional materials. For light propagating from an NZI material to conventional material (n_2), Snell's law relates the indices of refraction and refracted angle by $n_{\mathrm{NZI}} \sin\theta_{\mathrm{NZI}} = n_2 \sin\theta_2$. The incidence of a plane wave under any angle from the NZI side of the interface results in refraction only along the normal to the interface in the second medium. Reciprocally, refraction of a plane wave incident from the conventional medium in the NZI space can be correctly defined only for normal incidence, as oblique incidence will result in complete reflection. On the contrary, for normal incidence, Fresnel's coefficients are defined through intrinsic impedances $\eta = \sqrt{\mu\mu_0/\varepsilon\varepsilon_0}$, and in the absence of magnetic properties can be expressed through the refractive indices of materials in contact:

$$r = \frac{\eta_2 - \eta_1}{\eta_2 + \eta_1} = \frac{n_1 - n_2}{n_1 + n_2}, \tag{6a}$$

$$t = \frac{2\eta_2}{\eta_2 + \eta_1} = \frac{2n_1}{n_1 + n_2}. \tag{6b}$$

Without losses, the transmission (reflection) coefficient becomes either 2 (1) or 0 (-1) depending on whether a plane wave incidents from the air (n_1) on the NZI medium (n_2) or vice versa. We took the Drude model parameters of an ITO film from [10] and reduced the collision frequency by 1000 times to consider an almost lossless material. The real parts of Fresnel's reflection and transmission coefficients are plotted in Fig. 7(a) for the air/ITO boundary case. $\Re(t) = 2$ at the zero-crossing wavelength $\lambda \approx 1240$ nm, which can be classified as ENZ and NZI simultaneously.

However, plotting the transmittance T and reflectance R for the boundary problem accordingly to formulas

$$R = \left|\frac{n_1 - n_2}{n_1 + n_2}\right|^2, \tag{7a}$$

$$T = \Re(n_2)\left|\frac{2n_1}{n_1 + n_2}\right|^2 \tag{7b}$$

shows that these spectral parameters do not exceed one. For the case of negligible losses, $n_2 = \sqrt{\varepsilon}$ is purely imaginary at wavelengths beyond the ENZ point, giving an evanescent wave with zero transmittance and unitary reflectance. Consequently, the real picture is not so trivial as the complexity of the material function is much extended. In Fig. 7(b), we plot the same spectra but for normal ITO film. There are no abrupt breaks in transmission/reflection spectra, slopes become flatter, and no

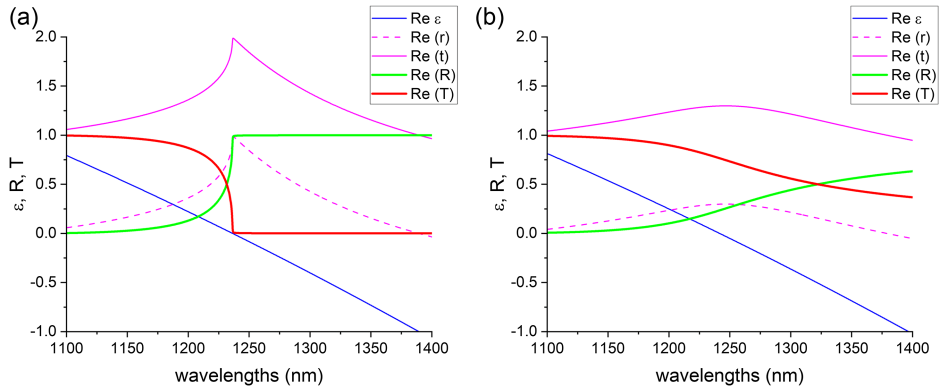

Fig. 7. Real parts of the dielectric function, reflection and transmission coefficients, transmittance, and reflectance at the interface between air and ITO. (a) Lossless case and (b) normal ITO.

extreme behavior is associated with the ENZ wavelength besides the maximum in the real part of the transmission coefficient.

4. WAVE PHENOMENA IN NZI MATERIALS

A fundamental property of propagating light is its phase, which is related to the variation of a wave cycle. In the absence of free charges and considering only time-harmonic fields ($E(t)$, $H(t) \propto e^{-i\omega t}$), the phase is given by the argument of the field function ($\mathbf{k}\cdot\mathbf{r} - \omega t + \phi$), where ϕ is a relative phase term that influences the spatial distribution of the wave. When the phase difference between two waves is kept constant, such waves are coherent and thus able to interfere. Conventionally, decoherence mechanisms are related to interaction with matter, with additional random phase changes modulating the signal. For a wave propagating inside an NZI material, the phase gets spatially constant due to negligible wavenumber k, having essential implications in undulatory phenomena such as diffraction and interference.

As light momentum is connected to the wave nature of electromagnetic waves, we start this discussion by introducing the description of momentum inside low-index media. Typically fundamental radiation processes are described by the energy exchange between light and matter, as shown by Einstein. Since the energy and momentum of a photon are directly connected, we can elaborate more on the link between these two quantities. Considering a simple two-level atomic system, the processes of absorption and emission of a quantum of energy $\hbar\omega$ coexist with a momentum transfer $\hbar\omega/c = \hbar k$ between the field and the atom, where $\hbar$ is the reduced Planck constant. Inside any material, the momentum of electromagnetic radiation depends on the refractive index. In a dispersive medium, one should distinguish between the conventional refractive index $n(\omega) = \sqrt{\varepsilon(\omega)\mu(\omega)}$ known as the phase refractive index, and the group refractive index $n_g = c\left(\frac{d\omega}{dk}\right)^{-1} = n + \omega\frac{dn}{d\omega}$.

Within such a framework, two formulations of the momentum are important to understand the role of the material properties (refractive indices) in light–matter interactions. The Abraham momentum (p_A) considers the corpuscular nature of light, whereas the Minkowski momentum (p_M) considers its wavelike nature. In a dispersive medium, the quantities are given by

$$p_A = \frac{\hbar\omega}{n_g(\omega)c}, \tag{8a}$$

$$p_M = n(\omega)\frac{\hbar\omega}{c}. \tag{8b}$$

Although NZI materials represent a wider category of materials with the real part of the refractive index being less than one, for the momentum considerations, the values of p_A and p_M will vary for ENZ, MNZ, and NZI media. As a consequence, at the zero-index frequency ω_Z, $n_g = \infty$ for ENZ and MNZ cases, and $n_g = \omega_z\frac{dn}{d\omega}$ for the NZI one. This also means that the group velocity will be zero for ENZ and MNZ materials, but nonzero for NZI. The Minkowski momentum will be zero for all three categories, as $n = 0$. Having a zero Minkowski momentum means that a photon does not transfer momentum to the matter inside an NZI material. The lack of p_M provides the means to understand the absence of a radiative process inside NZI materials since the momentum exchange between an atom and matter is forbidden. Such an effect was also described by Lobet *et al.* [26] within the framework of energy considerations of radiative processes.

Exhibiting a nonzero Abraham momentum for NZI materials means that although radiative processes are inhibited, electromagnetic radiation is still allowed to propagate inside the medium. Light–matter interactions demand conservation of the total momentum, connecting the Abraham and Minkowski momenta by the expression

$$p_{\text{kin}}^{\text{medium}} + p_A = p_{\text{can}}^{\text{medium}} + p_M, \tag{9}$$

which includes the sum of the kinetic momentum of the particle (p_{kin}) and the Abraham momentum of light from one side and the sum of the canonical momentum of the particle (p_{can}) and the Minkowski momentum of light from another. The canonical momentum is related to the de Broglie relation by $p_{\text{can}} = h/\lambda$. Therefore, the solution to the Abraham–Minkowski debate relies on the NZI environment giving different results for particle-oriented and wave-oriented experiments. The Abraham momentum considers the particle nature of light, whereas the Minkowski momentum is related to the wavelike nature of light. The full resolution to this dilemma can be found in [27].

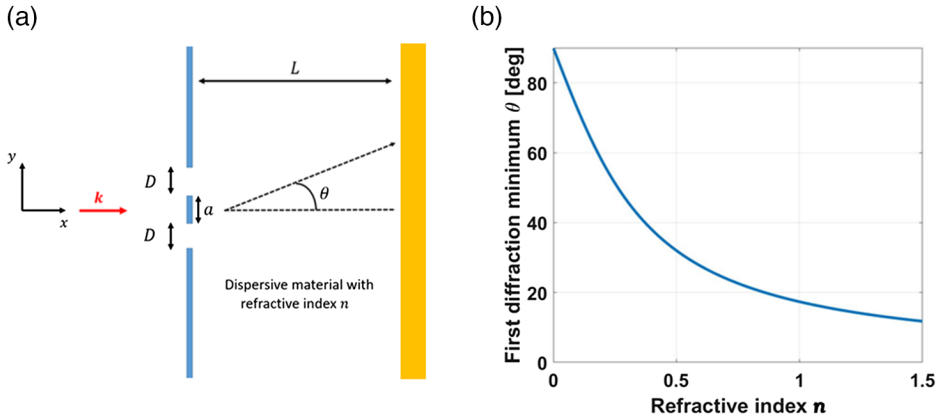

Fig. 8. (a) Incoming electromagnetic wave is sent on a double-slit screen with slit width D. The distance between slits is a, and the distance to the image plane is L. (b) First diffraction minimum as a function of the refractive index. Wavelength is set to 500 nm for a separation width of $a = 800$ nm.

An important observation can be made with the well-known Young's double slit experiment. A coherent light source is placed behind a nontransparent screen with two slits, and the generated light pattern is recorded at some distance at the other side of the screen. If the slits are surrounded by a conventional material, such as air, intensity fringes will appear on the screen due to diffraction and interference. However, such a pattern disappears if the surrounding environment is composed of a low-index material. We can explain this effect by looking at the diffraction condition. Let us consider the double-slit experiment, with slits of width D separated by a distance a. The distance between the screen with the slits and the observing plane is denoted as L, as illustrated in Fig. 8(a). The full system, including the screen, is embedded inside a dispersive medium with refractive index n. For $L \gg a$, the angle θ to the first diffraction minimum is given by the diffraction theory

$$\tan\theta = \frac{\lambda_0}{2a|n|}. \tag{10}$$

For media with a positive refractive index ($n > 1$), the diffraction angle is lowered by a factor $|n|$. Consequently, the intensity fringes get spatially closer, as shown in Fig. 8(b). In this situation, the corresponding canonical momentum p_x increases by the same factor. Nonetheless, if we decrease the refractive index approaching the NZI regime ($n < 1$), the canonical momentum tends to zero, and the first diffraction minimum moves away from the center, resulting in largely displaced fringes. The intensity distribution of the fringes on the image plane follows the expression

$$I(y) = \frac{I_0 \sin^2\left(\frac{\pi D y}{\lambda L}\right)}{2\left(\frac{\pi D y}{\lambda L}\right)}\left(1 + \cos\left(\frac{2\pi a y}{\lambda L}\right)\right), \tag{11}$$

where I_0 is the intensity of the incident wave, λ is the wavelength in the medium, and y is the vertical coordinate on the plane. As the refractive index approaches zero in Eq. (11), the effective wavelength tends to infinity and the cosine term to one. Therefore, $I \to I_0$, that is, the intensity on the image plane appears as a constant distribution, confirming that other orders of diffraction are removed to infinity. The same conclusions hold for single-slit experiments. Intuitively, we can think of the disappearance of the fringes as a consequence of the enlargement of the wavelength inside NZI materials. It is known that diffraction occurs on structures with sizes comparable to the wavelength. As the wavelength tends to infinity for ($n \ll 1$), diffraction effects are lost in the image plane as fringes are more and more spaced.

Another interesting conclusion arises from Babinet's principle, stating that the diffraction patterns of complimentary objects (a single slit and a rectangular object) should be similar. The suppression of the diffraction pattern inside NZI materials justifies the lack of scattering from an object with the dimensions of the slit. Consequently, the object is rendered invisible, and NZI material works as a cloaking mechanism. Cloaking corresponds to incertitude on the position of the invisible object, which corroborates the discussion above.

Our considerations of the double-slit experiment were verified by full-wave simulations as shown in Fig. 9. We simulate the diffraction pattern with four different surrounding materials: air

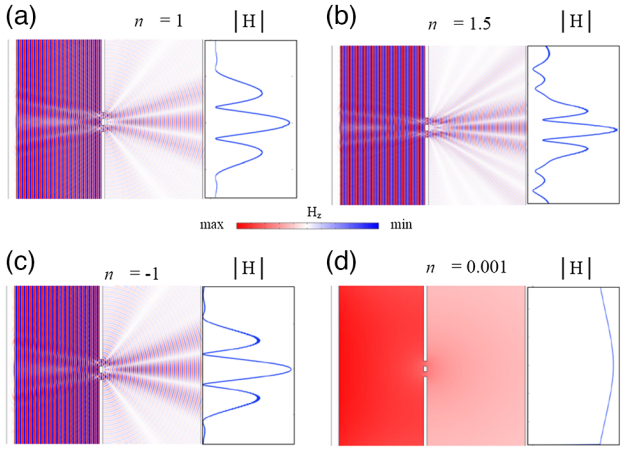

Fig. 9. Left panels: H_z field maps; right panels: $|H|$ profile at the image plane. (a) Air surrounding ($\epsilon = \mu = 1$, $n = 1$), (b) glass ($\epsilon = 2.25$, $\mu = 1$, $n = 1.5$), (c) negative refractive index material ($\epsilon = \mu = -1$, $n = -1$), and (d) NZI material ($\epsilon = 1.0 \times 10^{-6}$, $\mu = 1$, $n = 0.001$). Wavelength is set to 500 nm for a separation width of 800 nm.

($\epsilon = \mu = 1$, $n = 1$), glass ($\epsilon = 2.25$, $\mu = 1$, $n = 1.5$), negative refractive index material ($\epsilon = \mu = -1$, $n = -1$), and an NZI material ($\epsilon = 1.0 \times 10^{-6}$, $\mu = 1$, $n = 0.001$). As evidenced by the simulations, the diffraction patterns are not influenced by the sign of the refractive index but by its absolute value.

As mentioned previously, inside NZI materials, electromagnetic radiation experiences an enlargement of the wavelength. Such a spread of the position space brings important considerations in the Heisenberg uncertainty principle $\Delta p \Delta y \geq h$. The canonical momentum of the photon in an NZI material reduces to zero as $\Delta p = |n| \Delta p_0$. Since $|n_|| \approx 0$, we have $\Delta p \approx 0$. As a result, the exact knowledge of the momentum value leaves it with no uncertainty, imposing an infinite uncertainty in the position. In other words, the particle is delocalized, confirming its wavelength is infinite inside the NZI material.

5. APPLICATIONS OF NZI MATERIAL IN QUANTUM PHOTONICS

In this section, we point out some examples of rich potential applications of NZI materials for quantum systems, emphasizing radiative decay dynamics and coherent communication between distant emitters embedded in NZI materials.

A. Quantum Emitters and Decay Dynamics in NZI Materials

We start by considering a quantum emitter, for instance, a quantum dot, located in a cavity formed by an NZI material. Such a cavity will have its eigenfrequency overlapping with the atomic transitions of the quantum emitter. As demonstrated by Liberal *et al.*, the interaction between a two-level system and the NZI background becomes equivalent to a single-mode cavity [2]. As discussed previously, electromagnetic radiation in the NZI medium exhibits a decoupling between spatial and temporal variables. This means that the shape of the cavity will not influence the eigenfrequency. In conventional systems, when an emitter is placed inside a cavity, the population of electronic levels presents reversible dynamics with the Rabi frequency defined by the size of the cavity. Deforming such a cavity would result in the weakening of the Rabi oscillations due to the shift in the resonance frequency. Since the deformation of the cavity shape in an NZI material will not affect its eigenfrequency, we are able to tune the Rabi oscillations without detuning its resonance frequency. Such results bring novel possibilities to manipulate quantum states and their decay dynamics [28,29].

Another interesting discussion relies on the fundamental radiative processes inside NZI media and their dependence on dimensionality. As approached by Lobet *et al.* [26], materials with vanishing refractive indices will influence the decay dynamics of quantum emitters, such as the interaction between light–matter through spontaneous emission, stimulated emission, and absorption. Einsteins' coefficients A_{21}, B_{21}, and B_{12} calculate the rate of such processes, respectively. Considering a two-level system described by ground and excited states, the spontaneous emission was calculated via the Green function formalism by

$$A'_{21}(\omega) = \frac{2\omega^2}{\hbar \varepsilon_0 c^2} |\mathbf{p}|^2 \mathbf{u_z} \cdot \Im(\mathbf{G}(r_0, r_0, \omega)) \cdot \mathbf{u_z}$$

$$= \Re(\mu(\omega)\varepsilon(\omega)) A_{21}, \tag{12}$$

where $\mathbf{p} = p\mathbf{u_z}$ is the transition dipole moment, $\mathbf{G}$ is the Green function, and $A_{21} = \omega^3 |\mathbf{p}|^2/(3\pi\varepsilon_0 c^3)$ is the free-space spontaneous emission coefficient. For $n \to 0$, the spontaneous emission is inhibited in all NZI categories. Stimulated emission and absorption are also calculated through the Green function with the complete mathematical description found in [26]. As both processes are related to the density of states, the conclusion is that for unbounded 3D NZI media, all fundamental radiative processes are inhibited due to the depletion of optical modes around the NZI frequency. This result shows how the environment can tailor the radiative processes. The authors also introduce a unified framework in terms of dimensionality and conclude that it is crucial to consider both the number of optical modes that may couple to an emitter and the coupling strength. These parameters will depend on the NZI class and the number of spatial dimensions. For example, when analyzing the Purcell factor, in most NZI classes, spontaneous emission is inhibited. However, an enhanced Purcell factor is predicted inside 1D ENZ materials. Such conclusions have important implications for manipulating emitters' properties for quantum technologies.

B. Supercoupling Effect with Distant Emitters

A way to enable communication of separated emitters is extremely important in quantum information, communication, and computation. To finalize our considerations regarding applications of NZI materials in quantum photonics, we look at the exotic phenomenon known as the supercoupling effect as a way to allow communication between distant emitters. Normally dipole–dipole interactions between emitters are restricted to sub-wavelength distances. The supercoupling effect is a way to overcome this limitation; see Fig. 6.

Classically, the propagation of electromagnetic modes inside waveguides depends on the constituent materials and geometry. Abrupt bends, different cross sections, and unwanted scatterers caused by fabrication imperfections can deteriorate the transmitted signal. A counter-intuitive phenomenon occurs when very distorted waveguides are filled with an NZI material. For such waveguides, we could argue that the wavelength is extremely large and neither diffraction nor reflection from such structural parameters is sensed by light [30]. This effect is known as supercoupling. A stricter explanation lies within matching the impedance conditions. Impedance is a physical constant that relates the electric and magnetic fields through the equation

$$\eta = \frac{E}{H} = \sqrt{\frac{\mu}{\varepsilon}} \tag{13}$$

and is associated with a resistance to the propagation of waves. When a waveguide has different cross sections, an incoming wave suffers large reflection due to an impedance mismatch. However, this can be circumvented by inserting a narrow NZI material between waveguides, as illustrated in Fig. 10, where the

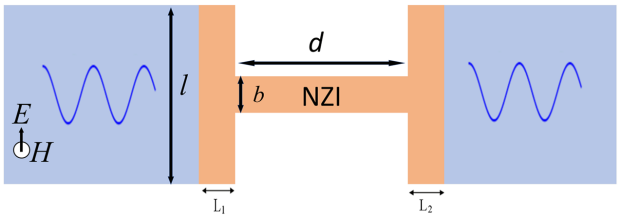

Fig. 10. Illustration of the impedance difference at the ports of a waveguide with a narrow NZI channel of length $d + L_1 + L_2$, coded in orange. The blue color represents a hollow waveguide.

wave tunneling through will experience matching of channels' impedances.

In this system, an incoming electric field polarized in the y direction, E_y, propagates through a hollow waveguide and is transmitted through an NZI waveguide with variable cross sections and lengths. We use Faraday's law $\oint \mathbf{E} \cdot \mathrm{d}\mathbf{l} = -\frac{d\Phi}{dt}$ to calculate the electric field at both ends of a narrow channel. The complete mathematical derivation of such a system can be found in [31–33]. The main results show that for waveguides of arbitrary cross sections (l_1 and l_2), a general formula for the reflection coefficient is given by

$$r = \frac{(l_1 - l_2) + ik_o\mu_r A}{(l_1 + l_2) - ik_o\mu_r A}, \tag{14}$$

where $A = (L_1 + L_2)l + bd$ is the cross-sectional area of the ENZ waveguide. From this equation, it follows that to minimize reflection, both waveguides should have the same cross section $l_1 = l_2$ at both ends and minimal area A, as predicted before.

The supercoupling effect is also possible even in channels with several fabrication imperfections due to the ability of waves not to react to obstacles. As a consequence of the enlargement of the wavelength, the wave will not experience the medium's deformities, therefore exhibiting enhanced transmission properties inside deformed waveguides [34]. We have performed simulations for the supercoupling effect using the commercially available software COMSOL Multiphysics [35], based on the finite element method.

In Fig. 11, we depict simulation results for tapered waveguides filled with an NZI material of refractive index $n = 0.001$. Figures 11(a) and 11(b) represent the results for NZI channels of $b = 20$ nm and $b = 300$ nm, where reflectance values of $R = 0.04$ and $R = 0.39$ were obtained, respectively. The same simulation was also performed for a very distorted waveguide in Fig. 11(c), where almost the same transmission was observed as for the straight channel of the same width.

The reflectance through a low-index channel of variable width ($20\ \text{nm} < b < 300\ \text{nm}$) and fixed length $d = 2\ \mu$m is shown in the plot of Fig. 12, with the lowest value of 4% corresponding to the narrowest channel. The blue curve in Fig. 12 represents the analytical results for the reflectance taken from the reflection coefficient Eq. (14). A small deviation from the complete transmission is predicted because the channel area would have to approach zero width. Such a configuration would make no sense since a waveguide is used to transmit the wave; thus, a small impedance mismatch is expected. A way to get around this is also to have μ close to zero, where a very small

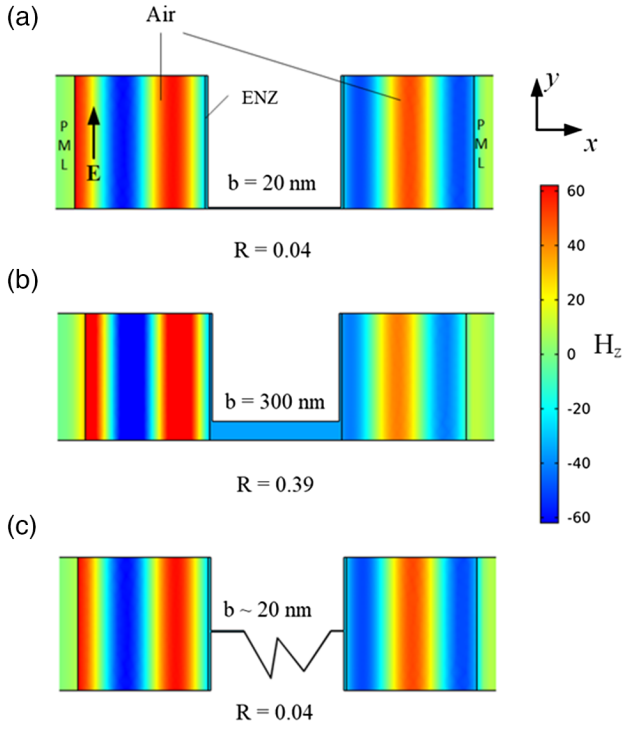

Fig. 11. (a) Supercoupling effect observed in a hollow waveguide with a narrow region filled with an ENZ material of width 20 nm and 2 μm length. For an incident electric field polarized in the y direction, 4% of reflectance was measured, while for a thicker channel of 300 nm, depicted in (b), the reflectance was 39%. In (c), we show that for the narrowest channel, even big deformities give a small reflection.

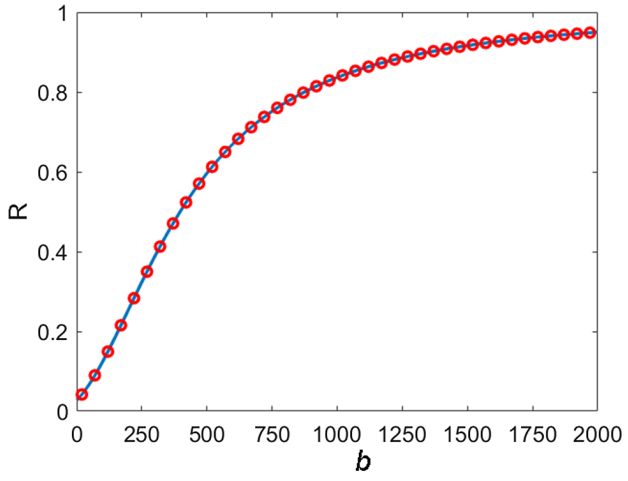

Fig. 12. Plot of the reflectance for an ENZ waveguide with variable cross section b and fixed length $d = 2\ \mu$m, where the red circles represent retrieved data from the simulation, and the blue curve is the analytical solution obtained through the reflection coefficient from Eq. (14).

value of permeability would be able to match the impedance for any channel thickness.

As suggested, we can now modify the system used to analyze the supercoupling effect to include emitters linked by NZI waveguides. With the direct contact of a source with a dissipative medium, the power radiated by the emitter has a singularity,

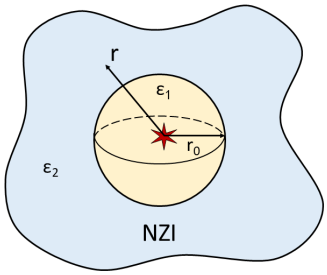

Fig. 13. Sketch of the system being considered for calculation of resonance conditions of an electromagnetic point source (red) placed at the center of a dielectric insertion (ε_1) surrounded by an NZI material (ε_2).

so it is not able to sustain its oscillations. Therefore, to allow continuous emission from a dipole into the NZI channel, it has to be placed first inside a dielectric insertion [36,37]. The dielectric material should be surrounded by an NZI material, as depicted in Fig. 13. Due to the high contrast between refractive indices, the NZI material will effectively form a cavity where the emission can be enhanced by fitting the size of the cavity to the right resonance conditions [28].

An electromagnetic field excited by a dipole can be written as a sum of transversal electric (TE) and TM modes. When the dipole is placed inside a dielectric sphere (ε_1) of radius r_0 immersed in an NZI material (ε_2), the internal fields are

$$\mathbf{E_{int}} = \sum_{\{q\}} [i a_{jm}^{l\mathrm{TM}} \mathbf{N}_{jm}^{l} - a_{jm}^{l\mathrm{TE}} \mathbf{M}_{jm}^{l}], \tag{15a}$$

$$\mathbf{H_{int}} = \frac{1}{\eta} \sum_{\{q\}} [a_{jm}^{l\mathrm{TM}} \mathbf{M}_{jm}^{l} + i a_{jm}^{l\mathrm{TE}} \mathbf{N}_{jm}^{l}], \tag{15b}$$

where $\{q\} = \{j, m, l\}$ are indices for the spherical harmonics. $\mathbf{M}_{jm}^{l}$ and $\mathbf{N}_{jm}^{l}$ are the vectors

$$\mathbf{M}_{jm}^{l} = \frac{1}{k} \nabla \times (\hat{B}_j(kr))\, T_{jm}^{l}(\hat{\boldsymbol{r}})\hat{\boldsymbol{r}}, \tag{16a}$$

$$\mathbf{N}_{jm}^{l} = \frac{1}{k} \nabla \times \mathbf{M}_{\mathbf{jm}}^{\mathbf{l}}, \tag{16b}$$

and

$$T_{jm}^{l}(\hat{\boldsymbol{r}}) = P_j^m(\cos(\theta))[\delta_{le}\cos(m\phi) + \delta_{lo}\sin(m\phi)]\hat{\boldsymbol{r}}, \tag{17}$$

where P_j^m are the Legendre polynomials, and $\hat{B}_j(kr) = (1 + c_{jm}^{l})\hat{J}_j(kr) + i\hat{Y}_j(kr)$ is a spherical Bessel function related by the cylindrical Bessel function of the first kind J_j of order n in the Schelkunoff form with $\hat{J}_j(x) = \sqrt{\pi x/2} J_{j+1/2}(x)$. $\hat{Y}_j$ are the spherical Bessel functions of the second kind, and c_{jm}^{l} are coefficients. Indices e and o represent even and odd modes for the Tesseral harmonics T_{jm}^{l} [38], respectively. The main idea behind this calculus is to find the coefficients for both TE and TM cases that would maximize the fields inside the sphere. This step is done by applying the boundary condition $\hat{\boldsymbol{n}} \times \mathbf{E} = 0$, which assures that the tangential fields will be continuous on the surface of the cavity, leading to the following sets of equations:

$$\frac{\hat{Y}_j'(k_2 r)\hat{J}_j'(k_2 r_0) - \hat{J}_j'(k_2 r)\hat{Y}_j'(k_2 r_0)}{\hat{Y}_j'(k_2 r)\hat{J}_j(k_2 r_0) - \hat{J}_j'(k_2 r)\hat{Y}_j(k_2 r_0)} = \frac{\eta_1}{\eta_2}\frac{\hat{J}_j'(k_1 r_0)}{\hat{J}_j(k_1 r_0)} \quad \text{(TM)}, \tag{18a}$$

$$\frac{\hat{Y}_j(k_2 r)\hat{J}_j(k_2 r_0) - \hat{J}_j(k_2 r)\hat{Y}_n(k_2 r_0)}{\hat{Y}_j(k_2 r)\hat{J}_j'(k_2 r_0) - \hat{J}_j(k_2 r)\hat{Y}_j'(k_2 r_0)} = \frac{\eta_1}{\eta_2}\frac{\hat{J}_j(k_1 r_0)}{\hat{J}_j'(k_1 r_0)} \quad \text{(TE)}, \tag{18b}$$

which represent the characteristic equations for TM and TE modes, respectively; k_1 and k_2 correspond to the wavenumbers for media 1 and 2. In the limit where ($\varepsilon_2 \to 0$) and the NZI volume is much bigger than the cavity, the above equations can be simplified as

$$-n = \frac{\varepsilon_2}{\varepsilon_1}(k_1 r_0)\frac{\hat{J}_n'(k_1 r_0)}{\hat{J}_n(k_1 r_0)} \quad \text{(TM)}, \tag{19a}$$

$$\frac{-1}{n} = \frac{1}{k_1 r_0}\frac{\hat{J}_n(k_1 r_0)}{\hat{J}_n'(k_1 r_0)} \quad \text{(TE)}. \tag{19b}$$

These calculations are based on multipole expansions, where a dipole source corresponds to the first order ($j = 1$). For the TM case, the field reaches the resonance condition with the highest value, when $\hat{J}_1(k_1 r_0) = 0$, while for TE modes, the condition is $\hat{J}_1'(k_1 r_0) = 0$. Therefore, by knowing the characteristic equations for both modes, we are able to determine the size of the dielectric sphere to put the system in resonance. In our case, the simulations of the supercoupling effect were performed considering the emission spectrum of a typical GaAs quantum dot [39], where the wavelength of our NZI material should be around 780 nm. To reach a magnetic dipolar resonance (TM mode), the radius of the air sphere $\varepsilon_1 = 1$ was $r = 110$ nm. The NZI material was chosen to have a small permittivity in both real and imaginary parts ($\varepsilon = 10^{-3} + i10^{-3}$).

The width, length, and height of the channel are flexible parameters, and we fix them to 10 nm, 1 μm, and 2 μm, respectively. A 100 nm thick layer of Au surrounding the waveguide was used to prevent radiation leakage to the environment [31]. The system was modeled by the commercially available software COMSOL [35]. In Fig. 14, we present the results for full 3D simulations, where the electric field produced by a quantum emitter simulated as a point source placed at the center of the left cavity is transmitted through a distorted ENZ waveguide. On the other side, an empty cavity is placed to monitor the transmitted field. The normalized electric field profile is collected along the red straight line in Fig. 14(b), displaying a decrease of 14% from one cavity to another, as shown in Fig. 14(b).

Since NZI channels can transmit electromagnetic radiation with a uniform phase, the geometry of the system has no strong influence on the phase distribution. We could have had more bends and an arbitrary displacement of the second cavity from the center of the NZI medium, but still achieve the same result due to the geometry invariance property of the NZI material [2]. Such flexibility enables more extended frames of nanophotonic device design.

The radiation of a quantum emitter with dipole moment **d** transmitted with high efficiency through the deeply subwavelength NZI waveguide makes it possible to excite another emitter with the same emission frequency in the other cavity. As

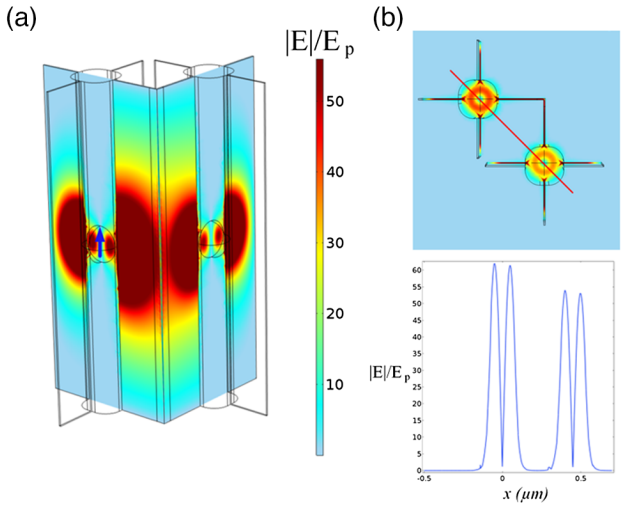

Fig. 14. (a) Electric dipole (blue arrow) is placed inside a spherical air cavity, of radius 110 nm, embedded in the NZI material, of 2 μm height. The color scheme represents the normalized electric field profile. For better visualization, the gold layer is not displayed. (b) The right figures show the top view with a cut line linking the two cavities (red) and the electric field profile along the red line.

we know, the quantum emitter can be modeled as a two-level system, and using the Green function approach combined with the formalism of master equations [40], we can compute the decay rate induced by mutual interactions between the two emitters ($\mathbf{d_1}$, $\mathbf{d_2}$) due to coupling:

$$\Gamma_{21} = \frac{2k_0^2}{\hbar\varepsilon_0}\mathbf{d_2}\cdot\Im(\mathbf{G}(\mathbf{r_2},\mathbf{r_1},\omega))\cdot\mathbf{d_1}, \tag{20}$$

where $(\mathbf{G}(\mathbf{r_2},\mathbf{r_1},\omega))$ is the Green's electric field tensor [41], calculated with the electric field retrieved by numerical simulations. A frequency shift due to dipole–dipole interactions (the Lamb shift) was also calculated according to [42,43]

$$\Delta\omega_{21} = \frac{-k_0^2}{\hbar\varepsilon_0}\mathbf{d_2}\cdot\Re(\mathbf{G}(\mathbf{r_2},\mathbf{r_1},\omega))\cdot\mathbf{d_1}. \tag{21}$$

The dipoles were placed in cavities with a 2 μm distance from each other. Both functions (the decay rate and Lamb shift) evidence cooperative behavior. Their plots are depicted in Fig. 15, where the decay rate and Lamb shift related to coupling are normalized by the free space decay rate. At the plasma frequency, we observe that the cooperative decay rate reaches a maximum, so the dipoles are effectively coupled.

The cooperative behavior in a system considering two emitters can be extended to multiple quantum emitters, as demonstrated by Mello *et al*. [44]. Although not subjected to the supercoupling effect, the authors show the effect of superradiance within many-body configurations due to the large spatial coherence inside NZI materials. An ultrahigh superradiant decay rate enhancement is verified. This result opens up future opportunities for quantum technologies, for example, decoherence-free quantum computation.

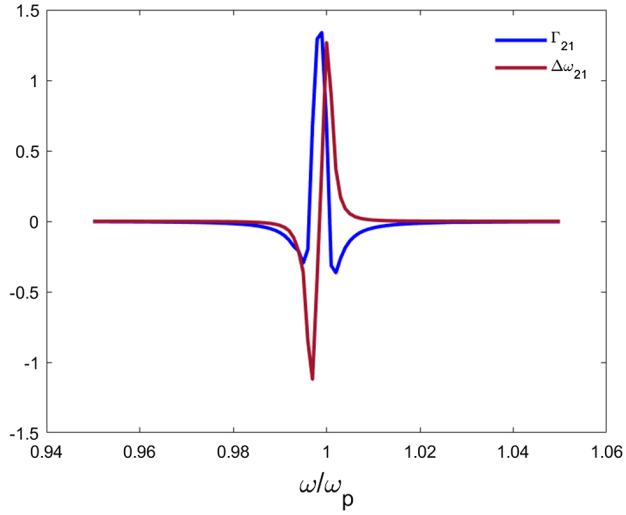

Fig. 15. Decay rate (blue) and Lamb shift (red) of two dipoles, embedded in an ENZ waveguide, normalized by the free space decay rate, as a function of the frequency normalized by the plasma frequency.

6. NONLINEAR PROPERTIES OF NZI MATERIALS

Nonlinear optical properties of ENZ materials have been in focus for almost a decade. Several papers provide indisputable evidence that thin layers of ENZ materials drastically increase the nonlinear response even without nanoengineering. The question under discussion is what is the physical origin of the enhanced ENZ nonlinearities. A thorough analysis of possible reasons is given in a recent review [7]. Though the review is dedicated to transparent conducting oxides (TCOs), such as ITO, AZO, and GZO, its discussion on the nature of ENZ nonlinearities can be extended to all classes of ENZ materials. Moreover, as TCOs are behind most advances reported with ENZ-enhanced nonlinearities, they are currently the main suspects for all ENZ-related nonlinear optics. This is promoted by the fact that their zero-crossing point is 1.0–3.6 μm and can be effectively tuned by fabrication conditions and doping levels.

From the first view, the ENZ and NZI points in TCOs almost coincide. Thus, the mixing of ENZ and NZI properties looks reasonable. Most of the nonlinear experiments in the generation of high harmonics or multi-wave mixing have actually been done at the ENZ wavelengths assuming that (i) it is very accurately defined, and (ii) losses, especially in pulsed laser deposited TCOs, are relatively low [45]. However, when nonlinear characterization is extended over a broader spectral range beyond the ENZ band, new factors pop up.

First, as mentioned in [46], the maximum refractive index change under Kerr nonlinearity in an AZO sample is recorded at $\lambda = 1390$ nm, or 90 nm redshifted from the ENZ point. The four-wave mixing (FWM) leading to the emission of back-propagating phase-conjugated waves and forward-propagating negative refracted waves reaches its maximal efficiency at wavelengths longer than the zero-crossing point [47]. A clear connection with low-index spectral behavior is shown while comparing the efficiency plot with the ellipsometry-retrieved refractive index data. The degenerated case of the refractive

index change under strong pumping is described in [48]. The difference in the real and imaginary parts of the third-order susceptibility results in different shifts of the maximum change in the real and imaginary parts of the refractive index. Both quantities are shifted towards the longer wavelengths from the zero-crossing point, being separated by about 100 nm at rather low pumping intensities in comparison with the non-degenerated case in [46]. One more reference reporting the frequency shifting in the degenerated FWM in an AZO film directly refers to the fact that such a nonlinear process is more efficient at wavelengths longer than λ_{ENZ} [49]. In this particular case, the pump and signal wavelengths were redshifted by 50 nm. Very recently, another paper reported that the ENZ (zero-crossing point) is not the optimal nonlinear condition. In [50], the frequency-resolved optical gating technique is used to present the second and third harmonic generation (THG) in a 270 nm thick AZO film. The operational spectral NZI window extends for over 268 nm FWHM centering at 1340 nm, and the THG is evident across the whole window. The clear maximum in the THG is exposed at somewhere around 1350 nm, which is probably redshifted from the ENZ wavelength (linear AZO permittivity data are not provided in the paper).

AZO is not the unique material to exhibit the optimal efficiency redshifted from the ENZ point. The third and higher-harmonic generation in an In-doped CdO film extends well beyond the ENZ wavelength displaying the redshifted peaks near it [51]. The effect was observed for the third and fifth harmonics and interpreted as the photoinduced heating of conducting electrons. The model provides quite close results; however, we think that it is not the complete description, as we show the dependence on the refractive index further on. In support of this thesis, we refer to a recent paper that points to the enhancement of light–matter interactions over the whole extent of the low-index domain [11]. There, a linear spin–orbit coupling effect is studied, and no intensive pumping is applied to heat the electrons significantly. The spectral behavior of the right-handed to left-handed conversion efficiency shows that it extends from around the ITO ENZ wavelength 1240 nm beyond the red end of the measurement window at 1500 nm peaking at 1320 nm–80 nm away from the exact ENZ point. The authors connect such behavior with the complex Fresnel's coefficients, namely, with the interplay between the difference in TE-TM polarization transmission and phases. However, the effect continues over 1400 nm wavelengths, where, according to simulations, the difference in TE-TM transmission almost nullifies. We think that the explanation should be connected with the NZI effect, which spans a bandwidth of more than 300 nm and more with the very flat real part of the refractive index (Fig. 16). Moreover, Fresnel's coefficients in a nonmagnetic media are conveniently expressed through refractive indices and not permittivity.

To support this version, we performed brute-force simulations of the THG in a thin layer of AZO at a few different wavelengths starting from the ENZ point at 1432 nm. As seen from Fig. 17, the zero-crossing point in no way is the best choice for the enhanced high-harmonic generation. The efficiency peak happens at about 70 nm longer wavelengths ($\lambda = 1500$ nm) belonging to the NZI range. The red wing of the peak is rather flat, as the NZI curve becomes very flat in this

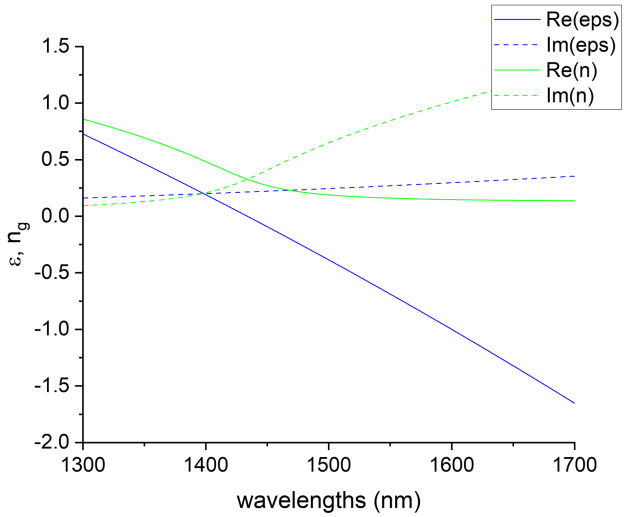

Fig. 16. Spectral behavior of AZO permittivity and refractive index. The Drude–Lorentz model was applied with coefficients from [6]. The ENZ point is at $\lambda = 1432$ nm. The low-index window extends over 1700 nm.

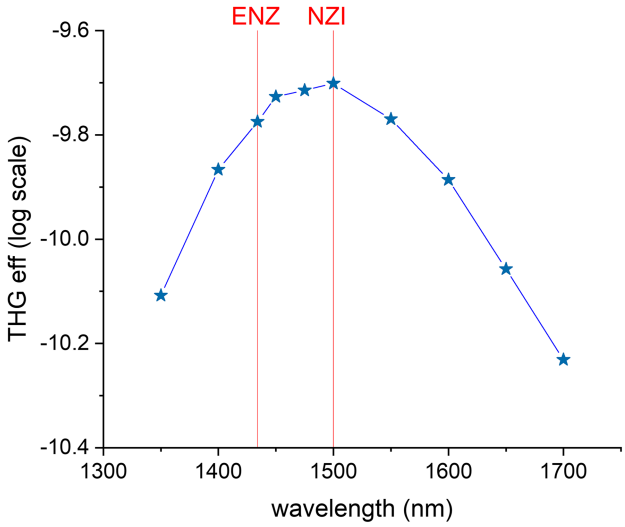

Fig. 17. Spectral behavior of THG efficiency in the logarithmic scale. The ENZ point is at $\lambda = 1432$ nm. The low-index window starts around 1500 nm and extends over 1700 nm.

range too. Certainly, the continuous growth of $\Im(n)$ reduces the efficiency towards the red part of the spectrum.

One reason for the ENZ enhancement of the nonlinear effects is connected with the amplification of the normal component of the electric field across the boundary. Hence, the effect can be optimized by changing the angle of incidence as validated in [10]. In our case, we use the normal incidence of a plane wave on a uniform layer, so the normal field component is absent by default, and such an argument in the nonlinear effects enhancement cannot be applied.

The reasoning behind the NZI enhancement regards the slow-light effect; see [7,52] and references therein. The group index is

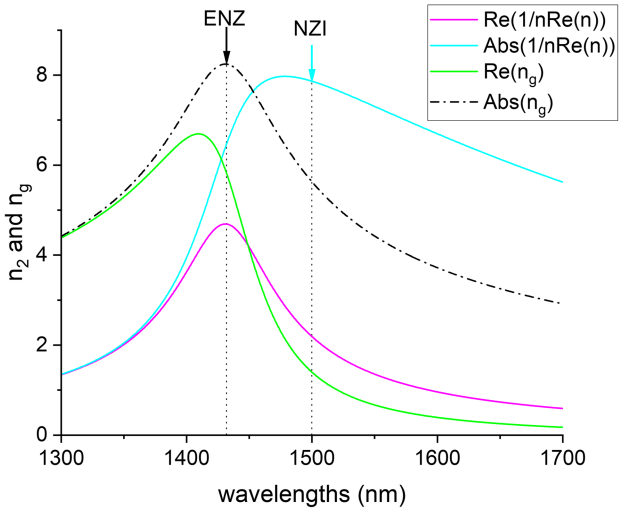

Fig. 18. Spectral behavior of the real and absolute values of the group index, and the real and absolute values of coefficient $1/n\Re(n)$.

$$n_g = \frac{\varepsilon(\omega) + \frac{\omega}{2}\frac{d\varepsilon(\omega)}{d\omega}}{\sqrt{\varepsilon(\omega)}}. \tag{22}$$

For most TCO materials, permittivity is accurately approximated by the Drude–Lorentz formula

$$\varepsilon(\omega) = \varepsilon_\infty - \frac{\omega_p^2}{\omega^2 + i\gamma\omega} + \frac{f_1\omega_1^2}{\omega_1^2 - \omega^2 - i\gamma_1\omega}, \tag{23}$$

where ε_∞, ω_p, and γ are conventional parameters of the Drude model, and ω_1, f_1 and γ_1 are those of the Lorentz term. Then, the group index Eq. (22) is derived with the following expression:

$$nn_g = \varepsilon_\infty - \frac{i\gamma\omega\omega_p^2}{2(\omega^2 + i\gamma\omega)^2} + \frac{f_1\omega_1^2(2\omega_1^2 - i\gamma_1\omega)}{2(\omega_1^2 - \omega^2 - i\gamma_1\omega)^2}. \tag{24}$$

Equation (24) can be drastically simplified to $nn_g = \varepsilon_\infty$ as in [52] in the case of negligible losses ($\gamma \ll \omega$) and neglecting the contribution of bound electrons ($f_1 = 0$). We took the material parameters of AZO from [6] and plot the group index's real part and absolute value in Fig. 18.

It is obvious that both the real part of the group index and its absolute value are peaking either even before the ENZ point ($\Re(n_g)$) or accurately at the ENZ point $|n_g|$, that is, $\Re(n_g) = \max$ at $\lambda = 1410$ nm and $|n_g| = \max$ at $\lambda = 1432$ nm. Therefore, the slow-light effect cannot unambiguously explain the nonlinear NZI material enhancement. As a notorious alternative explanation of the NZI enhancement, the perturbative formula

$$n_2 = \frac{3\chi^{(3)}(\omega)}{4n\Re(n)\epsilon_0 c} \tag{25}$$

can be applied within certain constraints. We plot the real and absolute values of the coefficient $1/n\Re(n)$ in Fig. 18 too. This coefficient, $|1/n\Re(n)|$, is a slow function of frequency, which reaches its maximum at $\lambda = 1481$ nm, or about 50 nm away from the zero-crossing point, actually, very close to the maximum of THG efficiency. In simulations, we use a direct

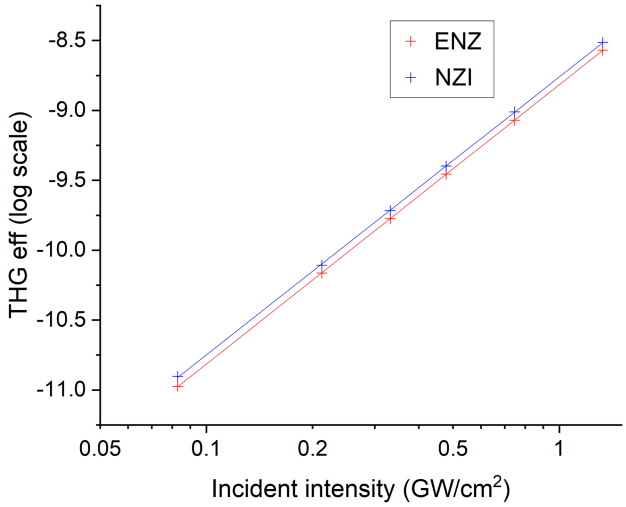

Fig. 19. Comparison of THG efficiency versus input power for two spectral points: ENZ point at $\lambda = 1432$ nm and the low-index point at $\lambda = 1500$ nm.

time-domain approach with the instantaneous Kerr nonlinearity realized in the Lumerical software package. Accordingly, no approximate formulas such as Eq. (25) are involved. The incident intensity was taken in the range 0.08−1 GW/ cm^2, which exhibits the range of levels where the perturbation theory is not yet compromised [53]. We think that the nonlinearity enhancement is due to the interplay of a few factors, among which the low refractive index (under reasonable losses) dominates.

To shed more light on the comparison of THG in a uniform sub-micrometer film at different wavelengths, we plot THG efficiency versus input intensity for $\lambda = 1432$ nm and $\lambda = 1500$ nm. As shown in Fig. 19, there is a small but constant difference in the high-harmonic generation efficiency in favor of the low-index regime over the ENZ regime.

7. CONCLUSION

In this tutorial, we analyze the behavior of NZI materials. We start by classifying materials according to their electromagnetic properties, specifying which conditions represent ENZ, MNZ, and NZI cases. However, the performance of ENZ materials is limited by their intrinsic losses related to the imaginary part of the permittivity, which refrains them from being defined as NZI materials. Therefore, we explore further an all-dielectric platform to overcome these losses.

Under the right circumstances, Mie resonances excited in a photonic crystal may have a degenerate point with three modes. This intercept is named Dirac's triple point, and at its frequency, the modes supported by the whole medium will behave as effectively having an NZI. We show results that prove the appearance of the effective NZI configuration in a conventional silicon photonic crystal. As expected, even with some deviations from the exact Dirac point, a propagating mode still can be characterized by a refractive index close to zero, and as such, exhibits the supercoupling effect illustrated in brute-force simulations. We anticipate that dielectric NZI materials represent a new step towards NZI platforms, where such structures pave the way to the reproducibility of zero-index effects that were suppressed by

intrinsic losses. As we illustrated in the tutorial, NZI materials expose a broad spectrum of interesting properties in different areas of optics and photonics, spanning from ray optics to nonlinear and quantum optics. In particular, building blocks of such materials can find implications in on-chip photonic circuitry, in the fields of biosensing, quantum photonics, and photonic engineering.

Funding. Danmarks Frie Forskningsfond (8022-00387B); Danmarks Grundforskningsfond (DNRF147).

Acknowledgment. LV and AL acknowledge support from the Danish National Research Foundation through NanoPhoton - Center for Nanophotonics. AL acknowledges support from the Independent Research Fund Denmark, DFF Research Project 2 "PhotoHub." MN acknowledges partial support from the Villum Fonden.

Disclosures. The authors declare no conflicts of interest.

Data availability. Data underlying the results presented in this paper are not publicly available at this time but may be obtained from the authors upon reasonable request.

REFERENCES

1. R. W. Ziolkowski, "Propagation in and scattering from a matched metamaterial having a zero index of refraction," Phys. Rev. E **70**, 046608 (2004).
2. I. Liberal, A. M. Mahmoud, and N. Engheta, "Geometry-invariant resonant cavities," Nat. Commun. **7**, 10989 (2016).
3. I. Liberal and N. Engheta, "Near-zero refractive index photonics," Nat. Photonics **11**, 149 (2017).
4. P. R. West, S. Ishii, G. V. Naik, N. K. Emani, V. M. Shalaev, and A. Boltasseva, "Searching for better plasmonic materials," Laser Photon. Rev. **4**, 795–808 (2010).
5. A. Boltasseva and H. A. Atwater, "Low-loss plasmonic metamaterials," Science **331**, 290–291 (2011).
6. G. V. Naik, V. M. Shalaev, and A. Boltasseva, "Alternative plasmonic materials: beyond gold and silver," Adv. Mater. **25**, 3264–3294 (2013).
7. W. Jaffray, S. Saha, V. M. Shalaev, A. Boltasseva, and M. Ferrera, "Transparent conducting oxides: from all-dielectric plasmonics to a new paradigm in integrated photonics," Adv. Opt. Photon. **14**, 148–208 (2022).
8. I. Liberal, A. M. Mahmoud, Y. Li, B. Edwards, and N. Engheta, "Photonic doping of epsilon-near-zero media," Science **355**, 1058–1062 (2017).
9. L. Brillouin, *Wave Propagation and Group Velocity* (Academic, 2013), Vol. **8**.
10. M. Z. Alam, I. De Leon, and R. W. Boyd, "Large optical nonlinearity of indium tin oxide in its epsilon-near-zero region," Science **352**, 795–797 (2016).
11. J. S. Eismann, L. Ackermann, B. Kantor, S. Nechayev, M. Z. Alam, R. Fickler, R. W. Boyd, and P. Banzer, "Enhanced spin-orbit coupling in an epsilon-near-zero material," Optica **9**, 1094–1099 (2022).
12. J. A. Briggs, G. V. Naik, Y. Zhao, T. A. Petach, K. Sahasrabuddhe, D. Goldhaber-Gordon, N. A. Melosh, and J. A. Dionne, "Temperature-dependent optical properties of titanium nitride," Appl. Phys. Lett. **110**, 101901 (2017).
13. H. Reddy, U. Guler, Z. Kudyshev, A. V. Kildishev, V. M. Shalaev, and A. Boltasseva, "Temperature-dependent optical properties of plasmonic titanium nitride thin films," ACS Photon. **4**, 1413–1420 (2017).
14. E. Shkondin, T. Repän, O. Takayama, and A. Lavrinenko, "High aspect ratio titanium nitride trench structures as plasmonic biosensor," Opt. Mater. Express **7**, 4171–4182 (2017).
15. L. Vertchenko, L. Leandro, E. Shkondin, O. Takayama, I. V. Bondarev, N. Akopian, and A. V. Lavrinenko, "Cryogenic characterization of titanium nitride thin films," Opt. Mater. Express **9**, 2117–2127 (2019).
16. Q. Zhao, J. Zhou, F. Zhang, and D. Lippens, "Mie resonance-based dielectric metamaterials," Mater. Today **12**, 60–69 (2009).
17. W. Hergert and T. Wriedt, *The Mie Theory: Basics and Applications* (Springer, 2012), Vol. **169**.
18. T. Wriedt, "Mie theory: a review," in *The Mie Theory* (Springer, 2012), pp. 53–71.
19. C. Chan, Z. H. Hang, and X. Huang, "Dirac dispersion in two-dimensional photonic crystals," Adv. OptoElectron. **2012**, 313984 (2012).
20. E. A. Novoselov and S. Kostya, "Two-dimensional gas of massless Dirac fermions in graphene," Nature **438**, 197–200 (2005).
21. X. Huang, Y. Lai, Z. H. Hang, H. Zheng, and C. Chan, "Dirac cones induced by accidental degeneracy in photonic crystals and zero-refractive-index materials," Nat. Mater. **10**, 582–586 (2011).
22. M. Minkov, I. A. Williamson, M. Xiao, and S. Fan, "Zero-index bound states in the continuum," Phys. Rev. Lett. **121**, 263901 (2018).
23. L. Vertchenko, C. DeVault, E. Mazur, and A. V. Lavrinenko, "Near-zero index photonic crystals with directive bound states in the continuum," Laser Photon. Rev. **15**, 2000559 (2021).
24. Y. Wu, J. Li, Z.-Q. Zhang, and C. Chan, "Effective medium theory for magnetodielectric composites: beyond the long-wavelength limit," Phys. Rev. B **74**, 085111 (2006).
25. A. Alu and N. Engheta, "Dielectric sensing in epsilon-near-zero narrow waveguide channels," Phys. Rev. B **78**, 045102 (2008).
26. M. Lobet, I. Liberal, E. N. Knall, M. Z. Alam, O. Reshef, R. W. Boyd, N. Engheta, and E. Mazur, "Fundamental radiative processes in near-zero-index media of various dimensionalities," ACS Photon. **7**, 1965–1970 (2020).
27. M. Lobet, I. Liberal, L. Vertchenko, L. Andrei, N. Engheta, and E. Mazur, "Momentum considerations inside near-zero index materials," Light Sci. Appl. **11**, 110 (2022).
28. I. Liberal and N. Engheta, "Nonradiating and radiating modes excited by quantum emitters in open epsilon-near-zero cavities," Sci. Adv. **2**, e1600987 (2016).
29. I. Liberal and N. Engheta, "Zero-index structures as an alternative platform for quantum optics," Proc. Nat. Acad. Sci. USA **114**, 822–827 (2017).
30. M. Silveirinha and N. Engheta, "Tunneling of electromagnetic energy through subwavelength channels and bends using ε-near-zero materials," Phys. Rev. Lett. **97**, 157403 (2006).
31. M. G. Silveirinha and N. Engheta, "Theory of supercoupling, squeezing wave energy, and field confinement in narrow channels and tight bends using ε near-zero metamaterials," Phys. Rev. B **76**, 245109 (2007).
32. B. Edwards, A. Alù, M. E. Young, M. Silveirinha, and N. Engheta, "Experimental verification of epsilon-near-zero metamaterial coupling and energy squeezing using a microwave waveguide," Phys. Rev. Lett. **100**, 033903 (2008).
33. L. Vertchenko, N. Akopian, and A. V. Lavrinenko, "Epsilon-near-zero grids for on-chip quantum networks," Sci. Rep. **9**, 6053 (2019).
34. B. Edwards, A. Alù, M. G. Silveirinha, and N. Engheta, "Reflectionless sharp bends and corners in waveguides using epsilon-near-zero effects," J. Appl. Phys. **105**, 044905 (2009).
35. COMSOL AB, "COMSOL multiphysics," http://www.comsol.com.
36. S. Scheel, L. Knöll, and D.-G. Welsch, "Spontaneous decay of an excited atom in an absorbing dielectric," Phys. Rev. A **60**, 4094 (1999).
37. C. Tai and R. E. Collin, "Radiation of a hertzian dipole immersed in a dissipative medium," IEEE Trans. Antennas Propag. **48**, 1501–1506 (2000).
38. R. Harrington, *Time-Harmonic Electromagnetic Fields* (McGraw-Hill, 1961).
39. G. E. Cirlin, R. Reznik, I. Shtrom, A. Khrebtov, I. Soshnikov, S. Kukushkin, L. Leandro, T. Kasama, and N. Akopian, "AlGaAs and AlGaAs/GaAs/AlGaAs nanowires grown by molecular beam epitaxy on silicon substrates," J. Phys. D **50**, 484003 (2017).
40. H. T. Dung, L. Knöll, and D.-G. Welsch, "Resonant dipole-dipole interaction in the presence of dispersing and absorbing surroundings," Phys. Rev. A **66**, 063810 (2002).
41. L. Novotny and B. Hecht, *Principles of Nano-Optics* (Cambridge University, 2012).

42. Y. Li, A. Nemilentsau, and C. Argyropoulos, "Resonance energy transfer and quantum entanglement mediated by epsilon-near-zero and other plasmonic waveguide systems," Nanoscale **11**, 14635–14647 (2019).
43. R. Sokhoyan and H. A. Atwater, "Quantum optical properties of a dipole emitter coupled to an epsilon-near-zero nanoscale waveguide," Opt. Express **21**, 32279–32290 (2013).
44. O. Mello, Y. Li, S. A. Camayd-Muñoz, C. DeVault, M. Lobet, H. Tang, M. Lonçar, and E. Mazur, "Extended many-body superradiance in diamond epsilon near-zero metamaterials," Appl. Phys. Lett. **120**, 061105 (2022).
45. A. Boltasseva and V. M. Shalaev, "All that glitters need not be gold," Science **347**, 1308–1310 (2015).
46. L. Caspani, R. P. M. Kaipurath, M. Clerici, M. Ferrera, T. Roger, J. Kim, N. Kinsey, M. Pietrzyk, A. Di Falco, V. M. Shalaev, A. Boltasseva, and D. Faccio, "Enhanced nonlinear refractive index in ε-near-zero materials," Phys. Rev. Lett. **116**, 233901 (2016).
47. S. Vezzoli, V. Bruno, C. DeVault, T. Roger, V. M. Shalaev, A. Boltasseva, M. Ferrera, M. Clerici, A. Dubietis, and D. Faccio, "Optical time reversal from time-dependent epsilon-near-zero media," Phys. Rev. Lett. **120**, 043902 (2018).
48. E. G. Carnemolla, L. Caspani, C. DeVault, M. Clerici, S. Vezzoli, V. Bruno, V. M. Shalaev, D. Faccio, A. Boltasseva, and M. Ferrera, "Degenerate optical nonlinear enhancement in epsilon-near-zero transparent conducting oxides," Opt. Mater. Express **8**, 3392–3400 (2018).
49. V. Bruno, S. Vezzoli, C. DeVault, E. Carnemolla, M. Ferrera, A. Boltasseva, V. M. Shalaev, D. Faccio, and M. Clerici, "Broad frequency shift of parametric processes in epsilon-near-zero time-varying media," Appl. Sci. **10**, 1318 (2020).
50. W. Jaffray, F. Belli, E. C. Carnemolla, C. Dobas, M. Mackenzie, J. Travers, A. K. Kar, M. Clerici, C. Devault, V. Shalaev, A. Boltasseva, and M. Ferrera, "Near-zero-index ultra-fast pulse characterization," Nat. Commun. **13**, 3536 (2022).
51. Y. Yang, J. Lu, A. Manjavacas, T. S. Luk, H. Liu, K. Kelley, J.-P. Maria, E. L. Runnerstrom, M. B. Sinclair, S. Ghimire, and I. Brener, "High-harmonic generation from an epsilon-near-zero material," Nat. Phys. **15**, 1022–1026 (2019).
52. J. B. Khurgin, M. Clerici, V. Bruno, L. Caspani, C. DeVault, J. Kim, A. Shaltout, A. Boltasseva, V. M. Shalaev, M. Ferrera, D. Faccio, and N. Kinsey, "Adiabatic frequency shifting in epsilon-near-zero materials: the role of group velocity," Optica **7**, 226–231 (2020).
53. O. Reshef, E. Giese, M. Z. Alam, I. De Leon, J. Upham, and R. W. Boyd, "Beyond the perturbative description of the nonlinear response of low-index materials," Opt. Lett. **42**, 3225–3228 (2017).